

NNT : \*\*\*

n°LAL : \*\*\*

Thèse de doctorat

# Search of the $0\nu\beta\beta$ decay with the SuperNEMO demonstrator

Thèse de doctorat de l'Université Paris-Saclay  
préparée à l'Université Paris Saclay au sein du Laboratoire Irène-Joliot Curie  
(anciennement Laboratoire de l'Accélérateur Linéaire)

École doctorale n°576 Particles, Hadrons, Energy, Nuclei, Instrumentation,  
Imaging, Cosmos et Simulation (PHENIICS)  
Spécialité de doctorat : Physique des particules

Thèse présentée et soutenue à Orsay, le \*\*\*, par

**CLOÉ GIRARD-CARILLO**

Composition du Jury :

\*\*\*

\*\*\*

Président

\*\*\*

\*\*\*

Rapporteur

\*\*\*

\*\*\*

Rapporteur

Christine Marquet  
CENBG - Bordeaux-Gradignan

Examineur

\*\*\*

\*\*\*

Examineur

\*\*\*

\*\*\*

Examineur

Laurent Simard  
LAL - Orsay

Directeur de thèse

Mathieu Bongrand  
LAL - Orsay

Co-directeur de thèse



---

# Contents

<b>Contents</b>	<b>3</b>
<b>Introduction</b>	<b>7</b>
<b>1 Phenomenology of particle physics</b>	<b>9</b>
1.1 The Standard Model of particle physics . . . . .	9
1.1.1 Bosons . . . . .	9
1.1.2 Fermions . . . . .	9
1.1.3 $2\nu\beta\beta$ decay . . . . .	9
1.1.4 Where the Standard Model ends . . . . .	9
1.2 Going beyond the Standard Model with neutrinos . . . . .	9
1.2.1 Neutrino flavors and oscillations . . . . .	9
1.2.2 Neutrino masses and nature . . . . .	9
1.2.3 Other searches beyond the Standard Model with neutrinos . . . . .	9
1.3 $0\nu\beta\beta$ experiment status . . . . .	9
1.3.1 Experimental design criteria . . . . .	9
1.3.2 $0\nu\beta\beta$ direct search experiments . . . . .	10
1.3.3 Bolometers . . . . .	12
1.3.4 Time projection chambers . . . . .	12
1.3.5 Scintillators . . . . .	14
1.3.6 Tracking calorimeters . . . . .	14
<b>2 The SuperNEMO demonstrator</b>	<b>15</b>
2.1 Demonstrator design . . . . .	15
2.1.1 Comparison with NEMO3 experiment . . . . .	15
2.1.2 Experimental design . . . . .	15
2.1.3 Sources . . . . .	15
2.1.4 Tracker . . . . .	15
2.1.5 Calorimeter . . . . .	15
2.1.6 Calibration systems . . . . .	15
2.1.7 Control Monitoring system . . . . .	15
2.1.8 Electronics . . . . .	15

2.2	The background of SuperNEMO . . . . .	15
2.2.1	Internal background . . . . .	15
2.2.2	External background . . . . .	17
2.2.3	Background specifications . . . . .	18
2.2.4	Measured demonstrator background levels . . . . .	18
2.3	Magnetic field . . . . .	18
2.4	The SuperNEMO software . . . . .	18
2.4.1	Simulation . . . . .	18
2.4.2	Reconstruction . . . . .	18
2.4.3	Modifications of simulation software . . . . .	18
2.5	Analysis tools . . . . .	18
2.5.1	Internal probability . . . . .	18
2.5.2	External probability . . . . .	20
<b>3</b>	<b>Sensitivity of the SuperNEMO demonstrator to the <math>0\nu\beta\beta</math></b>	<b>21</b>
3.1	The $0\nu\beta\beta$ signal and background model . . . . .	22
3.1.1	The $0\nu\beta\beta$ signal . . . . .	22
3.1.2	Inside detector backgrounds . . . . .	22
3.1.3	External backgrounds . . . . .	23
3.1.4	Amount of simulation . . . . .	24
3.2	Event selection . . . . .	25
3.2.1	Electron definition . . . . .	25
3.2.2	Total energy spectrum . . . . .	25
3.3	Demonstrator sensitivity to the $0\nu\beta\beta$ decay of $^{82}\text{Se}$ . . . . .	27
3.3.1	Sensitivity to the $0\nu\beta\beta$ half-life . . . . .	27
3.3.2	Limit on the effective neutrino mass . . . . .	29
3.4	Impact of sources contamination levels on the sensitivity . . . . .	31
3.4.1	Contamination levels . . . . .	31
3.4.2	Optimisation of event selection . . . . .	33
3.5	Impact of the magnetic field on the sensitivity . . . . .	39
3.5.1	Simulations of the magnetic field inside the demonstrator and reconstructed track fit . . . . .	40
3.5.2	Impact of the magnetic field on signal and background selections . . . . .	40
3.5.3	Influence of the magnetic field on optical modules and reconstruction efficiency . . . . .	43
3.5.4	Simulations with a non-uniform magnetic field . . . . .	44
3.6	Searching for the Neodymium-150 $0\nu\beta\beta$ decay . . . . .	45
3.6.1	Searching for the $0\nu\beta\beta$ of other isotopes . . . . .	45
3.6.2	Sensitivity to the $0\nu\beta\beta$ of $^{150}\text{Nd}$ . . . . .	45
3.7	The final detector sensitivity . . . . .	47
3.8	Conclusion . . . . .	48
<b>4</b>	<b>Improvement of the rejection of the internal Thallium-208 background</b>	<b>51</b>
4.1	Motivations . . . . .	51
4.2	The internal $^{208}\text{Tl}$ background . . . . .	52

4.2.1	The internal conversion process . . . . .	52
4.2.2	Selection of $^{208}\text{Tl}$ disintegrations in the 2e channel . . . . .	54
4.3	Rejection of $^{208}\text{Tl}$ with a time-of-flight criterion . . . . .	54
4.3.1	The internal probability . . . . .	55
4.3.2	The exponential probability for $^{208}\text{Tl}$ events . . . . .	57
4.4	Event selection . . . . .	59
4.4.1	Energy selection . . . . .	59
4.4.2	Arrival time cut-off . . . . .	60
4.4.3	Probability cut-off . . . . .	62
4.4.4	Selection optimisation . . . . .	65
4.5	Impact of $^{208}\text{Tl}$ rejection on the experiment's sensitivity . . . . .	65
4.5.1	Influence of the calorimeter time resolution . . . . .	65
4.6	Conclusions . . . . .	67
<b>5</b>	<b>Characterisation of the calorimeter time resolution</b>	<b>69</b>
5.1	Interaction of particles in the SuperNEMO scintillators . . . . .	70
5.1.1	Interaction of electrons . . . . .	70
5.1.2	Interaction of photons . . . . .	70
5.2	Measurement of the time resolution with a $^{60}\text{Co}$ source . . . . .	71
5.2.1	Description of Cobalt 60 nucleus . . . . .	72
5.2.2	Time response of optical modules . . . . .	72
5.2.3	Final experimental design . . . . .	75
5.2.4	Signal events selection . . . . .	77
5.2.5	Background estimation . . . . .	79
5.2.6	Detector efficiency . . . . .	83
5.2.7	Determination of the individual timing resolution of each optical module . . . . .	83
5.2.8	Conclusion . . . . .	88
5.3	The Light Injection System . . . . .	88
5.3.1	Light injection system commissioning . . . . .	89
5.3.2	Time resolution of optical modules . . . . .	89
<b>6</b>	<b>Detector commissioning</b>	<b>91</b>
6.1	Reflectometry analysis . . . . .	91
6.1.1	Goal of the reflectometry analysis . . . . .	91
6.1.2	Pulse timing: controlling cable lengths . . . . .	92
6.1.3	Signal attenuation . . . . .	97
6.1.4	Pulse shape analysis . . . . .	99
6.1.5	Comparison with $^{60}\text{Co}$ . . . . .	99
6.1.6	Conclusion . . . . .	99
6.2	Calibrating the electronic boards . . . . .	99
6.2.1	Principle . . . . .	99
6.2.2	Measuring the time offset of front end boards . . . . .	99
6.2.3	Results . . . . .	99
6.3	Energy calibration of optical modules . . . . .	99
6.4	Baseline studies . . . . .	99
6.5	Light Injection System . . . . .	99

## CONTENTS

---

<b>Conclusion</b>	<b>101</b>
<b>Bibliography</b>	<b>103</b>

## Improvement of the rejection of the internal Thallium-208 background

At the end of September 2018, the 34 enriched-Selenium source foils were installed on the demonstrator. At this time, the internal  $^{208}\text{Tl}$  and  $^{214}\text{Bi}$  activities had already been measured by the BiPo detector, as well as the  $^{222}\text{Rn}$  concentration inside the tracker chamber. We described in the previous chapter the impact of these activities on the final detector sensitivity to the  $0\nu\beta\beta$  decay, and set up optimised topological selections adjusted to reject the Radon background.

However, the  $^{208}\text{Tl}$  background also remains a troublesome source of background, even for  $\beta\beta$  emitters with a high  $Q_{\beta\beta}$ . Indeed, it contributes at high energies (up to 4 MeV on the two electrons energy sum spectrum), because of the internal conversion of the 2.615 MeV  $\gamma$ -ray. In a context where the  $^{208}\text{Tl}$  contamination is higher than expected, we focus in the current chapter on rejection techniques peculiarly adapted to reject internal  $^{208}\text{Tl}$  events. We study the influence of these techniques on  $0\nu\beta\beta$  events selection, and evaluate the impact on final detector sensitivity.

### 4.1 Motivations

In Chapters 2 and 3, we presented the specifications set on the background activities, in order to reach an unprecedented limit on the  $0\nu\beta\beta$  process half-life of the  $^{82}\text{Se}$  in 5 years, with 100 kg of the  $^{82}\text{Se}$  isotope, with the final SuperNEMO detector. Tab. 2.1 summarises the target  $^{208}\text{Tl}$ ,  $^{214}\text{Bi}$  and  $^{222}\text{Rn}$  activities, and give a comparison with those measured by the collaboration. We achieve the specified level of  $^{222}\text{Rn}$  isotope inside with an air flow rate of 2 m<sup>3</sup>/h inside the wire chamber. The BiPo detector was only capable of giving an upper limit on the  $^{214}\text{Bi}$  level of  $\mathcal{A}^{\text{Bi}} < 290 \mu\text{Bq/kg}$ , and future precise measurements with SuperNEMO demonstrator will constraint this value. The BiPo measurements also showed that the  $^{208}\text{Tl}$  contamination is about 30 times greater than expected. We give in Tab. 4.1 the number of expected background events for the measured activities (taking the upper limit for  $^{214}\text{Bi}$  contamination), for the demonstrator and final detector. The  $^{208}\text{Tl}$  level of activity has no implication for the demonstrator,

#### 4. IMPROVEMENT OF THE REJECTION OF THE INTERNAL THALLIUM-208 BACKGROUND

Exposure ROI (MeV)	Demonstrator 17.5 kg.y [2.7;3.3]	Detector 500 kg.y [2.6;2.95]
$2\nu\beta\beta$	0.383	104
$^{208}\text{Tl}$	1.09	21.2
$^{214}\text{Bi}$	1.42	110
$^{222}\text{Rn}$	0.0782	6.11

Table 4.1: Expected number of background events in optimised energy ranges for the SuperNEMO demonstrator (17.5 kg.y) and the final detector (500 kg.y exposure). The  $2\nu\beta\beta$  half-life is taken as  $T_{1/2}^{2\nu} = 9.39 \times 10^{19}$  y, and the measured background activities are considered (with the upper limit for  $^{214}\text{Bi}$  contamination). The topological selections have been optimised:  $P_{int} > 4\%$  and  $|\Delta Z| < 80$  mm.

as only one event is expected in the [2.7;3.3] MeV energy region, after cut-off optimisations, with a 17.5 kg.y exposure. On the other hand, this background could be harmful for the final detector, with 21  $^{208}\text{Tl}$  events expected in the region of interest [2.6,2.95] MeV, for a 500 kg.y exposure. To overcome this effect, it is interesting to set a specific method designed to reject  $^{208}\text{Tl}$  events.

In the next section, we describe the specific features of the Thallium internal background. We develop a new technique of rejection, especially designed to identify internal  $^{208}\text{Tl}$  events, based on electron Time-Of-Flight computation.

## 4.2 The internal $^{208}\text{Tl}$ background

Trace quantities of naturally-occurring radioactive isotopes inside the source foils can occasionally produce two-electron events, and thus can mimic  $\beta\beta$ -decay events. The  $^{208}\text{Tl}$ , a progeny of  $^{232}\text{Th}$ , is one of the largest contribution to the internal background. In fact, as explained in Chapter 2, two electrons can be produced via  $\beta$ -decay followed by a Møller scattering,  $\beta$ -decay to an excited state with the subsequent internal conversion, or due to Compton scattering of the de-excitation photon (Fig. 2.1).

All the possible transitions for the  $^{208}\text{Tl}$  isotope are presented in Fig. 4.1. This shows that  $^{208}\text{Tl}$  always  $\beta$ -decays to an excited state of the  $^{208}\text{Pb}$  daughter nuclei. In more than 99 % of the decays, at least 2  $\gamma$ 's are expected after the  $\beta$  emission. For  $0\nu\beta\beta$  detection, the most dangerous mode of  $\beta\beta$ -like events production comes from the internal conversion of the 2.615 MeV- $\gamma$ , resulting in two electrons emitted with a high energy sum.

### 4.2.1 The internal conversion process

An excited nucleus will practically constantly achieve a transition to a lower state by one of two processes: the emission of a  $\gamma$ -ray, or the ejection of one of the orbital electrons. The latter, called *internal conversion* (frequently abbreviated IC), is a second-order process, where one electron couples to one of the nucleon inside the



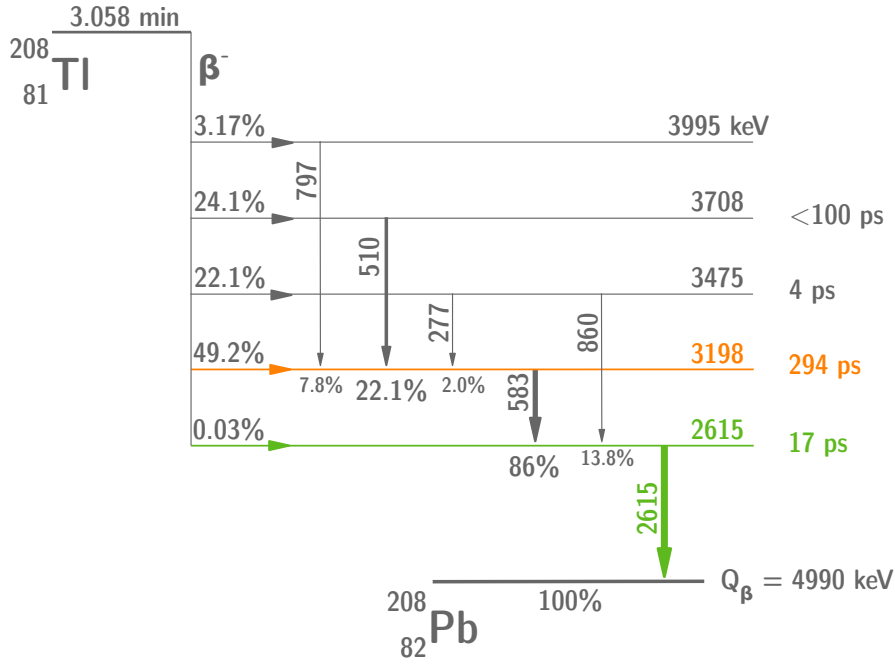


Figure 4.1: A simplified disintegration scheme for the  $^{208}\text{Tl}$  isotope. 81 % of the disintegration pass through the 294 ps metastable energy level (orange). All disintegration go through the 2.615 MeV energy level (green), where an orbital electron is ejected in 0.246 % of the cases through the internal conversion process.

excited nucleus. Thus, in such a radioactive decay, the de-excitation energy of the nucleus is transferred *directly* to a  $j$ -shell electron ( $j = K, L, M, \dots$ ). A high-energy electron is therefore emitted from the atom, and carry off the energy

$$E_{IC} = E_\gamma - E_j \quad (j = K, L, M, \dots), \quad (4.1)$$

where  $E_j$  is the binding energy of the electron in the  $j$ -shell, and  $E_\gamma$  is the energy of the  $\gamma$ -ray.

This mechanism is possible because there is a non-zero probability of finding the electron within the nucleus, that is to say, the wave-function of the electron can penetrate the volume of the nucleus. Consequently, due to their high nuclear penetration, electrons coming from the  $1s$  state are more likely to be ejected (this transition is called  $K$  internal conversion). Although electrons coming from  $2s$ ,  $3s$  and  $4s$  states ( $L$ ,  $M$  or  $N$  internal conversions) have also a non-zero probability to undergo this process. After the electron ejection, the hole in the corresponding shell is filled by an electron from a higher energy level, emitting characteristic X-rays, Auger electrons, or both.

For a given transition, the internal conversion coefficient of the electron in the  $j$ -shell, is defined by

$$\alpha_j = \frac{P_{IC,j}}{P_\gamma}, \quad (4.2)$$

where  $P_{IC,j}$  is the  $j$  conversion electron emission probability, and  $P_\gamma$  is the  $\gamma$ -ray

#### 4. IMPROVEMENT OF THE REJECTION OF THE INTERNAL THALLIUM-208 BACKGROUND

emission probability. The total coefficient is

$$\alpha_T = \sum_{j=K,L,M\dots} \alpha_j. \quad (4.3)$$

These coefficients are given in Tab. 4.2, for the 2.615 MeV energy level of the  $^{208}\text{Tl}$  decay scheme. Therefore, in 0.246 % of the cases, the  $^{208}\text{Pb}$  excited nucleus will

Emission probability (%)	$\alpha_K$ (%)	$\alpha_L$ (%)	$\alpha_M$ (%)	$\alpha_T$ (%)
100	0.1708	0.0292	0.00685	0.246

Table 4.2: Internal conversion coefficients for the 2.615 MeV  $\gamma$ -ray of the  $^{208}\text{Tl}$  decay scheme.

undergone an internal conversion corresponding to the 2.615 MeV energy level.

##### 4.2.2 Selection of $^{208}\text{Tl}$ disintegrations in the 2e channel

The  $^{208}\text{Tl}$  can present a 2e electrons topology, when after the  $\beta$  emission, an electron is ejected from the atom through internal conversion. Especially, when this energy transfer corresponds to the 2.615 MeV  $\gamma$ -ray, the ejected electron carry off a significant energy, depending on its initial binding energy with the nucleus. An orbital electron from the K-shell is ejected with an energy  $E_{IC,K} = 2.526$  MeV, for instance. In such a case, the  $^{208}\text{Tl}$  disintegration can be identified in the 2e topology. As one of the two electrons measured with a high energy, this decay is likely to contribute to the background of the  $0\nu\beta\beta$  of  $^{82}\text{Se}$ , or even  $^{150}\text{Nd}$ . In Fig. 4.2 is presented the individual energy spectra for 2e topologies for  $^{208}\text{Tl}$  simulations inside the source foils. An usual technique to reject  $^{208}\text{Tl}$  background consists in distinguishing 2e topologies for which one of the two calorimeter hit has an energy greater than 2.7 MeV. The energy resolution of the demonstrator being improved compared with the one of NEMO-3, this selection is efficient. This cut-off allow to reject 0.61 % of the  $^{208}\text{Tl}$  internal events, while rejecting only 0.11 % of  $0\nu\beta\beta$  events.

In the 2e channel, optimised topological cut-offs, based on time-of-flight computation and the distance between vertices, were presented in the previous chapter. They are mostly efficient in rejecting the non-internal  $^{222}\text{Rn}$  events. In the next section, we remind and precise the internal probability computation, and present a new selection, also based on the time-of-flight computation, to reject the  $^{208}\text{Tl}$  background.

### 4.3 Rejection of $^{208}\text{Tl}$ with a time-of-flight criterion

- Un des deux gamma est retardé de 294 ps, puis conversion interne -> donner la proportion de retardés (nb d'ev attendus, dans la ROI)

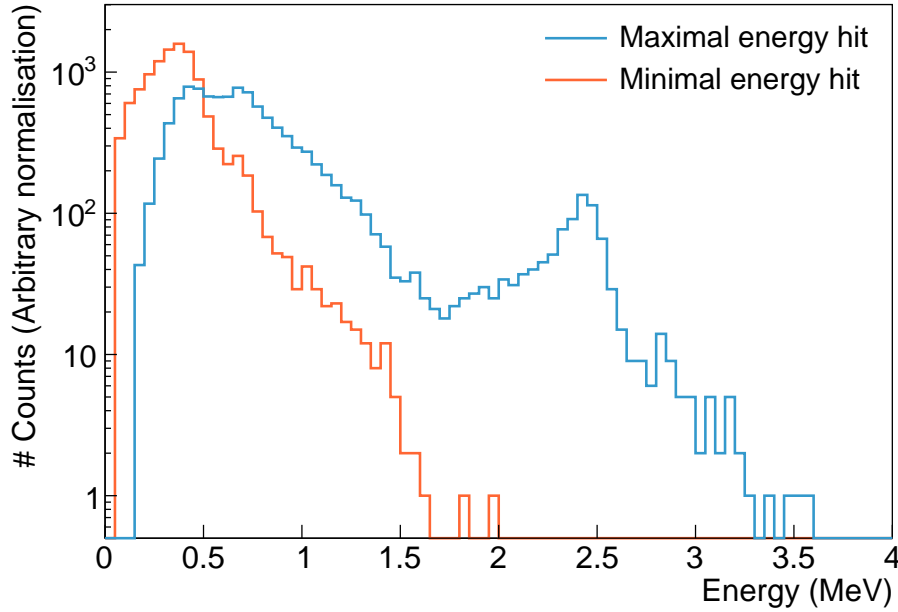


Figure 4.2: Individual energy spectra for selected 2e topologies of  $^{208}\text{Tl}$  decays simulated inside the source foils. Calorimeter hit of minimal energy (red) and maximal energy (blue). Spectra are arbitrarily normalised. The [2.7;3.2] ROI is represented by grey dashed lines.

- Avant d’entrer dans le détail préciser le principe de la réjection par temps de vol. L’électron de plus haute énergie est en retard, avec un retard en moyenne de 294 ps pour la plupart des niveaux (discuter un peu le schéma de désintégration, dans quel cas il sera en retard). Ensuite dire que tu as quantifié le pourcentage d’électrons de haute énergie en retard avec une simulation ”parfaite” i.e. avec une résolution en temps nulle. A comparer avec le chiffre donné précédemment (issu d’une étude du schéma de désintégration.)

### 4.3.1 The internal probability

This tool, which aims to reject non-simultaneous events, is presented in detail in Chapter 2. As part of the analysis pipeline, it is widely employed in NEMO-3 and SuperNEMO, for background rejection purposes. We examine an example of its usefulness in Chapter 3. Nevertheless, for reasons to be given latter, in the current chapter, we need to perform our own calculation of internal probability, after the reconstruction pipeline. That is an opportunity to come back to this tool and to clarify certain points. The calculation of the internal  $\chi^2$  is reminded in Eq. (4.4), for two detected electrons, as a function of the expected times,  $t^{\text{exp}}$ , the experimentally measured times,  $t^{\text{meas}}$ , as well as the total uncertainty on the time measurement:

$$\chi_{int}^2 = \frac{((t_1^{\text{meas}} - t_1^{\text{exp}}) - (t_2^{\text{meas}} - t_2^{\text{exp}}))^2}{\sigma_{t_1}^2 + \sigma_{t_2}^2 + \sigma_{\beta_2}^2 + \sigma_{\beta_1}^2 + \sigma_{t_1}^2 + \sigma_{t_2}^2}. \quad (4.4)$$

#### 4. IMPROVEMENT OF THE REJECTION OF THE INTERNAL THALLIUM-208 BACKGROUND

The components of the total time uncertainty are brought by the calorimeter performance ( $\sigma_{t_i}$ ), the uncertainty on particle energies ( $\sigma_{\beta_i}$ ) and the uncertainty on track lengths ( $\sigma_{l_i}$ ). In the official SuperNEMO reconstruction pipeline,  $\sigma_l = \sigma_{l_1} = \sigma_{l_2} = 70$  ps for electrons. As, therein chapter, we are predominantly focusing on the  $2e$  channel to reject the  $^{208}\text{Tl}$  background, we would optimise this parameter to describe accurately the internal events.

One way to examine if  $\sigma_l$  is well-evaluated is to look at the flatness of the internal probability distribution for  $0\nu\beta\beta$  events in the  $2e$  topology, for which a flat distribution is expected. Indeed, the slope of this distribution provides pertinent information to check the estimation of uncertainties. The flatter the distribution, the more correctly uncertainties are estimated. We perform a lineal fit of the  $P_{int}$  distribution on  $[0.1; 1]$ , to avoid the peak at low internal probabilities, and we define the *flatness parameter*  $a_F$  as the slope of this fit. The optimisation then consists in finding the value of  $\sigma_l$  for which the parameter  $a_F$  is cancelled. We compute the  $P_{int}$  distribution for simulations of  $0\nu\beta\beta$  decays inside the source foils. We select merely  $2e$  topologies by using the first order cuts, presented in Chapter 3, such that the internal hypothesis is almost certain to be verified. In Fig. 4.3 is given the slope  $a_F$  as a function of  $\sigma_l$ . For  $\sigma_l = 70$  ps,  $a_F > 0$ , revealing

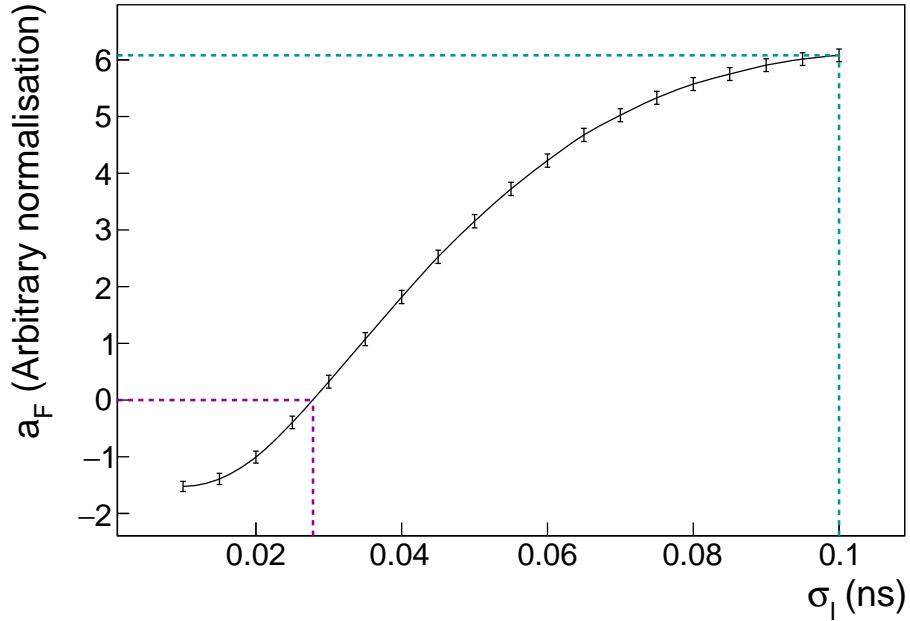


Figure 4.3: Slope  $a_F$  as a function of the time uncertainty due to the reconstructed track length  $\sigma_l$ . The former value used in the SuperNEMO reconstruction pipeline is pointed out by blue dashed lines. The value kept for  $\sigma_l$  is the one for which  $a_F = 0$ ,  $\sigma_l = 27.8 \pm 0.8$  ps, showed by purple dashed lines. The errors made on the  $a_F$  fit parameter are represented by the grey filled area.  $P_{int}$  is calculated for  $0\nu\beta\beta$  decays simulated inside the source foil, with first order cut-offs applied.

an overestimation of uncertainties in the computation of the internal  $\chi^2$ . The optimised value, kept for the further analysis, is  $\sigma_l = 27.8 \pm 0.8$  ps. In Fig. 4.4 is

displayed the internal probability distributions for two values of the  $\sigma_l$  parameter: for the former value  $\sigma_l = 70$  ps and for the optimised value  $\sigma_l = 0.0278$  ns. Let us notice that normally  $\sigma_L$  should depend on the track length as well as the

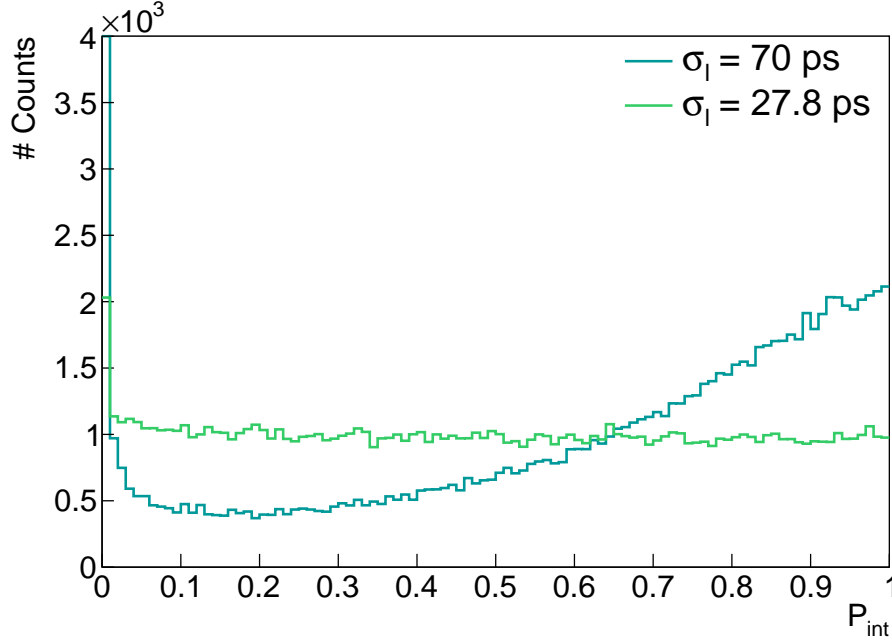


Figure 4.4: Internal probability distributions for  $\sigma_l = 70$  ps (blue) and  $\sigma_l = 27.8$  ps (green).  $P_{int}$  is calculated for  $0\nu\beta\beta$  decays simulated inside the source foil, with first order cut-offs applied.

energy, especially as multiple scattering in the tracker has a more notable impact for low energy electrons. A more complete analysis would compare the simulated track lengths with the reconstructed ones, for different energy sets of mono-kinetic electrons. Nevertheless, our optimisation is good enough for the current analysis. We use this optimisation for the rest of this analysis, and discussion is in progress to modify this parameter in the SuperNEMO software.

The internal probability is principally designed to reject non-simultaneous events coming from the source foil. Therefore, it is extremely effective in rejecting  $^{222}\text{Rn}$  events produced far from the source foils. The internal probability is however not suited for  $^{208}\text{Tl}$  disintegrations occurring within the foils, because of the metastable state could delay significantly the electron with higher energy. So we would set up a new law of probability that would express the hypothesis that a given event is an internal  $^{208}\text{Tl}$  event.

### 4.3.2 The exponential probability for $^{208}\text{Tl}$ events

According to the disintegration scheme of the  $^{208}\text{Tl}$  isotope (Fig. 4.1), there is an 81 % probability of passing through the 294 ps metastable level. After that, to attain the ground state of  $^{208}\text{Pb}$ , the excited nucleus has 100% of probability to decay through the 2.615 MeV energy level. At this occasion, in 0.246% of cases (Tab. 4.2), one of the orbital electrons is ejected from the atom following the

internal conversion process. To summarise, for 0.16 % of the total  $^{208}\text{Tl}$  decays, a  $\beta$  particle is emitted, and a delayed orbital electron is ejected through internal conversion of the 2.6 MeV- $\gamma$ . We aim to use this delayed electron to discriminate  $^{208}\text{Tl}$  internal background from the  $0\nu\beta\beta$  signal.

#### 4.3.2.1 Exponentially modified Gaussian

For a given  $^{208}\text{Tl}$  disintegration, we define the  $\Delta t$  parameter as the difference of arrival time between the firstly emitted  $\beta$  particle and the delayed IC electron. Supposing SuperNEMO would perfectly measure the particles' times and energies, the  $\Delta t$  probability density function would be an exponential, with the decay parameter  $\tau = 294$  ps. We introduced in Chapter 2 the internal probability analysis tool. At this occasion, let us described the components entering in the computation of the total uncertainty on time measurement for the SuperNEMO calorimeter. To take into account measurement uncertainties, we define a Gaussian distribution centred around  $\mu = 0$ , with a width set up by the  $\sigma = \sigma_{tot}$  parameter, detailed in Eq. (2.4). Therefore, to properly describe the  $\beta$ +IC delayed  $^{208}\text{Tl}$  events, we have to convolve the exponential and the Gaussian distributions.

#### 4.3.2.2 Probability density function

In Fig. 4.5 we show  $E \otimes G(\tau, \mu, \sigma)$ , the convolution of an exponential function and a Gaussian function. This density probability distribution corresponds to the case

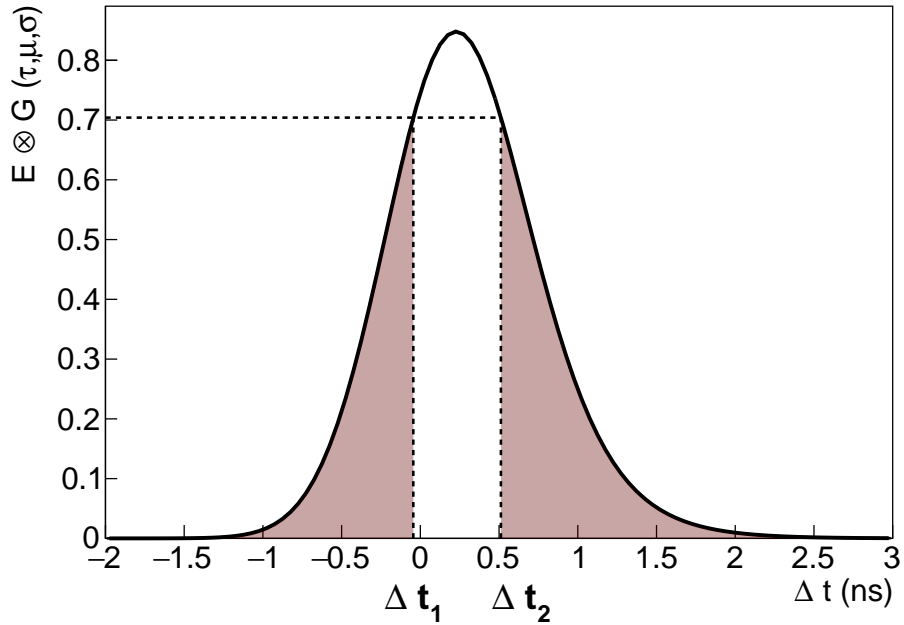


Figure 4.5: Normalised convolution distribution  $E \otimes G(\tau, \mu, \sigma)$ . The parameters are  $\tau = 294$  ps,  $\mu = 0$  ps and  $\sigma = \sigma_{tot}$ , computed with  $\sigma_l = 27.8$  ps and  $\sigma_t = 400$  ps.

where the two detected electrons were emitted through the  $\beta$ +IC delayed process, given a certain total uncertainty  $\sigma_{tot}$  on the arrival time measurement. For our

purpose, the parameter  $\tau$  corresponds to the decay-time of 294 ps of the  $^{208}\text{Tl}$  metastable energy level. The two parameters  $\mu$  and  $\sigma$  correspond to the mean and total uncertainty of the Gaussian function, respectively. In our case,  $\mu = 0$  ps and the total uncertainty is calculated with  $\sigma_l = 27.8$  ps and  $\sigma_t = 400$  ps. Each probability density function is unique and depends on the value of the measured energies for the two particles detected in the  $2e$  topology. In the given example, we considered two particles interacting inside the calorimeter with an energy of 1 MeV each. The  $E \otimes G(\tau, \mu, \sigma)$  distribution is normalised.

### 4.3.2.3 Exponential probability

Once the probability density function is built for a given  $2e$  event, we would define the probability  $P_e$  that this event comes from a  $\beta$ +IC delayed decay. We want to define the exponential probability following the same principle as for the internal probability, for comparison purposes. Therefore, we would obtain the maximal value  $P_e = 1$  when the value of  $\Delta t$  is the most favourable, i.e. when  $\Delta t$  is of the order of the mean of the  $E \otimes G(\tau, \mu, \sigma)$  distribution. On the other hand, minimal values for  $P_e$  would be reached for unfavourable values of  $|\Delta t|$ , so  $P_e \xrightarrow{|\Delta t| \rightarrow +\infty} 0$ .

Following these two requirements, the exponential probability is defined as

$$P_e = \int_{-\infty}^{\Delta t_1} E \otimes G(\tau, \mu, \sigma) dx + \int_{\Delta t_2}^{-\infty} E \otimes G(\tau, \mu, \sigma) dx, \quad (4.5)$$

where  $\Delta t_2$  is one of the two primitives of  $E \otimes G(\tau, \mu, \sigma)$  as  $f(\Delta t_1) = f(\Delta t_2)$ . [à changer] These two integrals are represented by coloured areas in Fig. 4.5. The same way as internal probability, exponential probability distribution is expected to be flat for  $^{208}\text{Tl}$  simulations on  $]0; 1]$ .

In fig. 4.6 is presented an exponential probability distribution for  $^{208}\text{Tl}$  and  $0\nu\beta\beta$  simulations inside the source foils, after first-order cut applied.

- Pour Laurent : il faut que l'on parle de cette distrib. Car elle n'est pas si plate que ça, notamment pour les petits Pexp, on a comme un excès

## 4.4 Event selection

The aim of this analysis is to set up a technique adapted to reject  $^{208}\text{Tl}$  events.

### 4.4.1 Energy selection

The lower bound of the region of interest for the search of  $0\nu\beta\beta$  decay stands at the electron energy sum 2.7 MeV. From this energy,  $2e$  topologies for  $^{208}\text{Tl}$  are mainly populated by  $\beta$  decays followed by the internal conversion of the 2.615 MeV  $\gamma$ -ray. In the following, we therefore focus only on events with a sum in energy of the two electrons greater than 2.7 MeV.

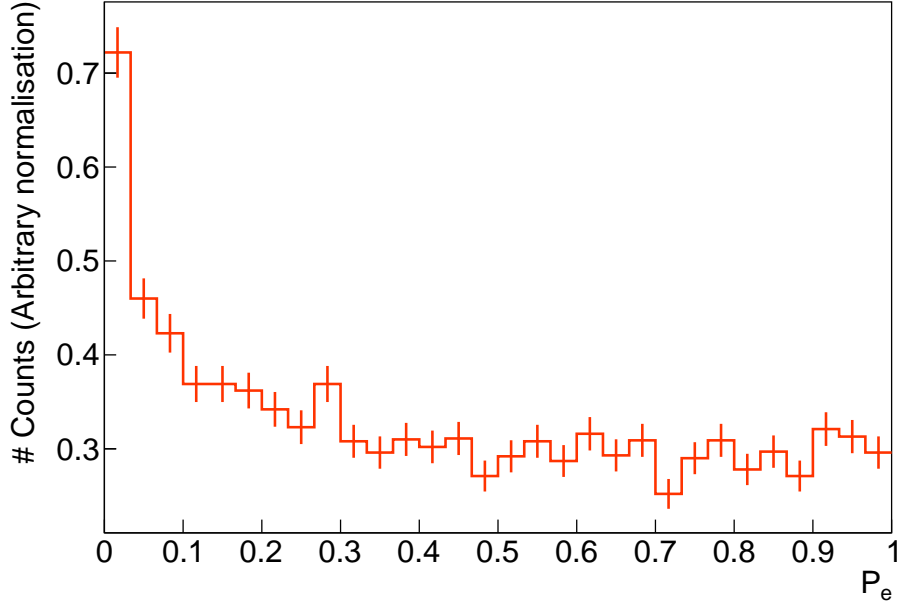


Figure 4.6: Exponential probability distribution for  $^{208}\text{Tl}$  simulations, after first-order cut-offs have been applied.  $\sigma_t = 400$  ps,  $\sigma_l = 27.8$  ps.

#### 4.4.2 Arrival time cut-off

We are especially focused on rejecting the internal  $^{208}\text{Tl}$  events for which the successive  $\gamma$ -rays emissions went through the 294 ps half-life metastable state. For these decays, we are expecting the particle of highest energy to be delayed compared with the one of lowest energy. Therefore, we consider the two electron arrival times inside the calorimeter for a given  $2e$  topology and we define the time difference between them as

$$\Delta t = t_1^{\text{meas}} - t_2^{\text{meas}}, \quad (4.6)$$

where the time  $t_1$  is the arrival time of the highest energy particle, and the time  $t_2$  designates the other. The time  $t_i^{\text{meas}}$  it takes for a particle to reach the calorimeter depends on how long it took for it to exit the source foils after emission, as well as to travel through the wire chamber. In order to remove from  $\Delta t$  the dependency on travel time in the tracker, we define the corrected time difference as

$$\Delta t^{\text{corr}} = t_1^{\text{corr}} - t_2^{\text{corr}} \quad (4.7)$$

$$= (t_1^{\text{meas}} - t_1^{\text{exp}}) - (t_2^{\text{meas}} - t_2^{\text{exp}}), \quad (4.8)$$

where  $t_i^{\text{corr}}$  are the measured arrival times  $t_i^{\text{meas}}$  corrected of the expected arrival times  $t_i^{\text{exp}}$  calculated with the particle energy and track length.

The two distributions  $\Delta t$  and  $\Delta t^{\text{corr}}$  are presented in Fig. 4.7, for  $0\nu\beta\beta$  and  $^{208}\text{Tl}$  simulations inside the source foils. For  $0\nu\beta\beta$  simulations, the  $\Delta t$  distribution is centred around zero, as the two electrons are expected to be emitted simultaneously. Then, the correction on time difference only lowers the standard deviation of the distribution. For  $^{208}\text{Tl}$  simulations, the mean of the  $\Delta t$  distribution



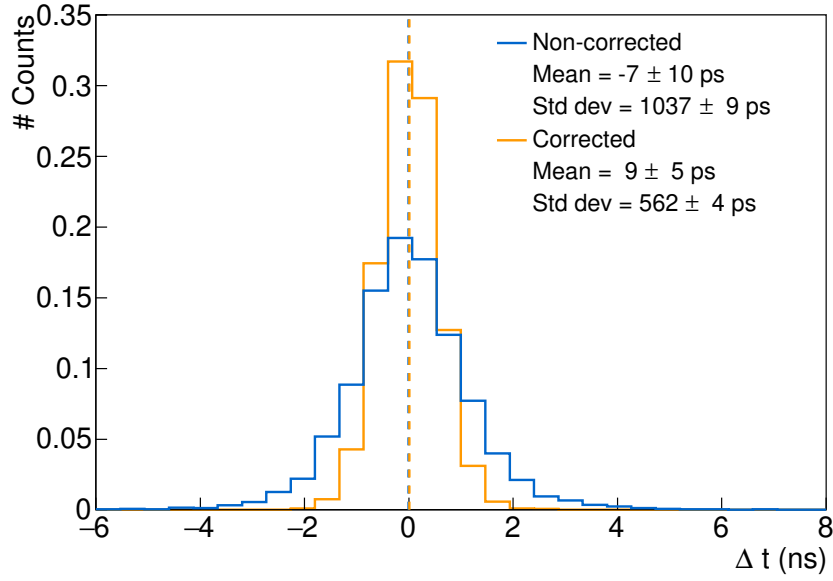
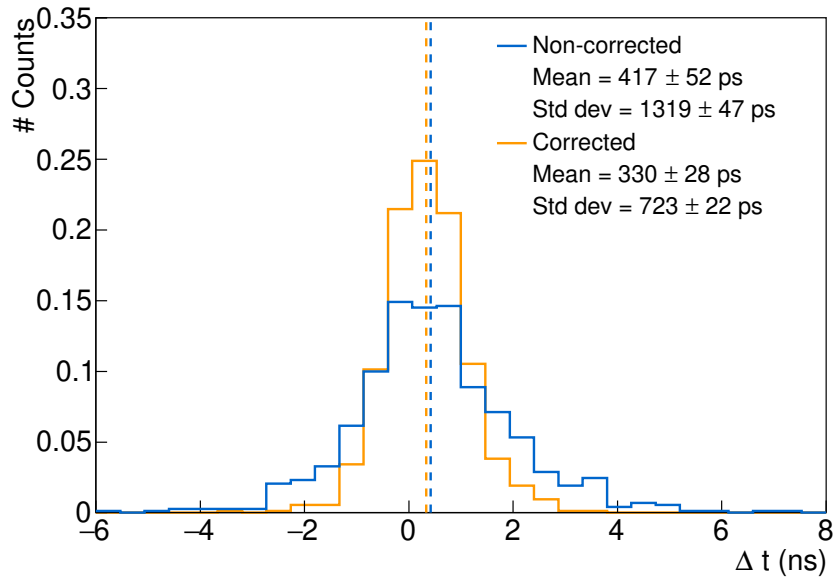
(a)  $0\nu\beta\beta$  simulations.(b)  $^{208}\text{Tl}$  simulations.

Figure 4.7: Corrected (orange) and non-corrected (blue) arrival time difference between the two electrons. (a)  $0\nu\beta\beta$  simulations inside the source foils. (b)  $^{208}\text{Tl}$  simulations inside the source foils. The first-order selections have been applied. The two distributions are normalised.  $\sigma_t = 400$  ps and  $\sigma_l = 27.8$  ps.

is slightly shifted towards positive values. Once corrected by the expected times, the mean difference between the two electrons arrival times stands at  $330 \pm 28$  ps. This is a direct consequence of the existence of  $\beta+\text{IC}$  delayed events, for which the particle of highest energy is expected to hit a calorimeter block at a time  $t_1^{\text{corr}} > t_2^{\text{corr}}$ . Therefore, a simple way of rejecting the  $^{208}\text{Tl}$  delayed events is to

consider the sign of  $\Delta t^{\text{corr}}$ : these events are more likely to have  $\Delta t^{\text{corr}} > 0$ . A simple cut-off consist in rejecting  $2e$  topologies for which  $\Delta t^{\text{corr}} > 0$ .

For an calorimeter time uncertainty of  $\sigma_t = 400$  ps, we are able to reject 67 % of  $^{208}\text{Tl}$  while selecting 50 % of the  $0\nu\beta\beta$ , for the  $2e$  topologies with  $E > 2.7$  MeV. Although we manage to reject a significant fraction of Thallium events, the impact of this cut is too high on  $0\nu\beta\beta$  events. We study in Sec. 4.4.4 an optimization of this cut-off, including the influence of the temporal performance of the calorimeter  $\sigma_t$ .

### 4.4.3 Probability cut-off

One of the main drawback of the cut on  $\Delta t^{\text{corr}}$  presented is that it does not take into account the uncertainties on time measurements. Two analysis tools were presented in Sec. 4.3. The first one, called internal probability, was already used in Chapter 3, and is a widely-used tool to reject non-simultaneous events, taking into account these uncertainties. The second was designed specifically for this analysis to identify delayed  $^{208}\text{Tl}$  events, and also depends on the uncertainties through the convolution with a Gaussian function.

A useful way of representing the probability cut-off is to display a two-dimensional binned histogram of  $P_e$  as a function of  $P_{\text{int}}$ , as done in Fig. 4.8. We

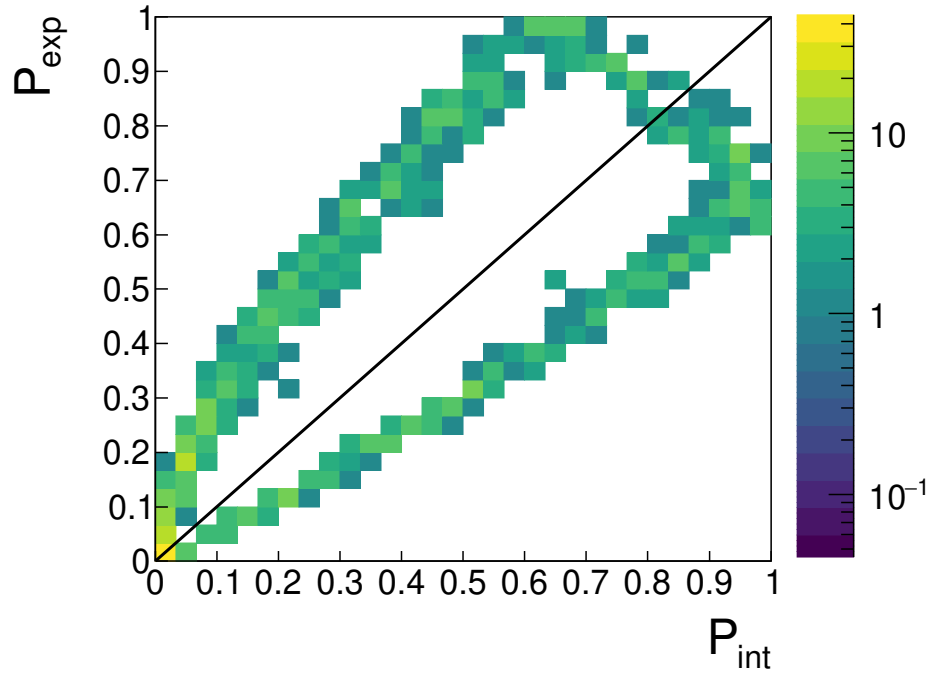


Figure 4.8: Two-dimensional histogram showing the  $P_e$  distribution as a function the  $P_{\text{int}}$  distribution, for  $^{208}\text{Tl}$  simulations.  $\sigma_t = 400$  ps and  $\sigma_l = 27.8$  ps. The first-order cut-off and the energy selection  $> 2.7$  MeV have been applied.

clearly distinguish three event populations in this histogram. In order to better

understand the variations in this histogram, we give in Fig. 4.9 three examples of  $E \otimes G$  distributions, one for each of the three zones.

1.  $P_{int} \in [0; 1]$  and  $P_e \in [0; 0.65]$  (Fig. 4.9a):

This region corresponds to events for which  $\Delta t^{\text{corr}} < 0$ . As the internal  $\chi^2$  distribution is symmetrical, such events can have a value of  $P_{int}$  varying from 0 to 1. Small values of  $P_{int}$  correspond to events with a large  $\Delta t^{\text{corr}}$  in absolute value. Conversely, the exponential distribution is not centred in zero. Therefore, if we limit to events for which the time difference is negative, we reach an upper bound for the value of the integral (0.65 in that case). This bound directly depends on the variations of the exponential distribution, therefore to  $\sigma_t$ .

2.  $P_{int} \in [0; 0.65]$  and  $P_e \in [0; 1]$  (Fig. 4.9b):

These events have positive values for  $\Delta t^{\text{corr}}$ , beyond the  $E \otimes G$  distribution maximum. The smaller the value of  $P_{int}$ , the lower the probability that both particles were emitted at the same time into the source. Besides, for values of  $\Delta t^{\text{corr}}$  highly positives, the value of the exponential probability can reach high values, up to 1. The larger the value of  $\Delta t^{\text{corr}}$  in positives, the smaller the value of  $P_e$ .

3.  $P_{int} \in [0.65; 1]$  and  $P_e \in [0.65; 1]$  (Fig. 4.9c):

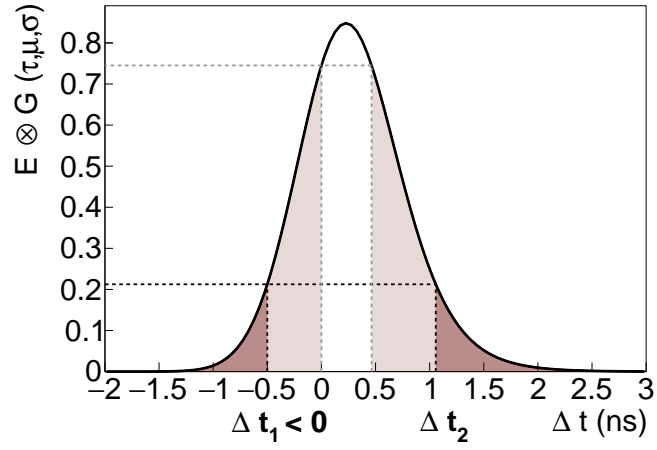
This region is also populated by events for which  $\Delta t^{\text{corr}} > 0$ . Unlike the previous case, these events have small  $\Delta t^{\text{corr}}$  values, meaning above the maximum of the exponential distribution. Also, these events have high internal probability values, as the probability that these two particles were emitted simultaneously is high. In the same way as the first item, the value of the integral is bounded: the lower bound corresponds to the value of the integral when  $\Delta t^{\text{corr}} = 0$  (here 0.65). Once again, this bound is deeply related to the value considered for  $\sigma_t$ . The exponential probability can be equal to 1 when  $\Delta t^{\text{corr}}$  reaches the maximum of the exponential distribution.

Therefore, the exponential probability not only tests the hypothesis that a detected event corresponds to delayed thallium, but also, as with internal probability, quantifies the probability that two particles were emitted simultaneously from the source foils.

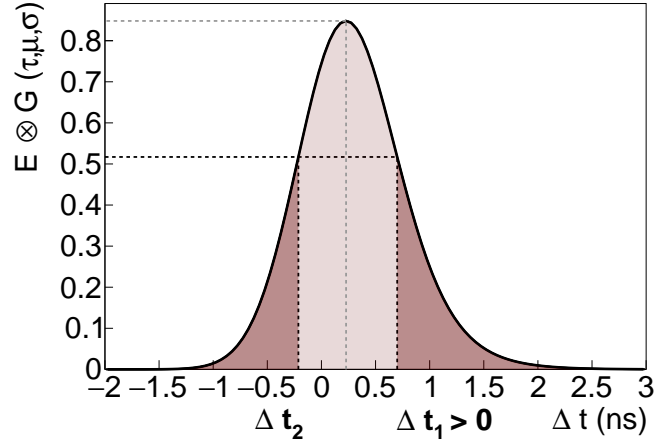
As we want to discriminate signal  $0\nu\beta\beta$  from delayed  $^{208}\text{Tl}$  events, we reject  $2e$  topologies for which  $P_e > P_{int}$  (this cut-off is also represented in Fig. 4.8). With the previous explanation, we understand that such a cut is strongly linked to the cut on  $\Delta t^{\text{corr}}$  presented in the previous sub-section. For  $\sigma_t = 400$  ps, we are able to reject 60% of  $^{208}\text{Tl}$ , while selecting 58% of  $0\nu\beta\beta$   $2e$  topologies for which  $E > 2.7$  MeV. Although we are able to keep more  $0\nu\beta\beta$  events with this probability cut-off than for the one on arrival time difference, this level is still not satisfying. Moreover, at first glance, this cut-off is less efficient than the  $\Delta t$  cut-off in rejecting  $^{208}\text{Tl}$  events. However, it is much more interesting to consider a cut on event probability rather than a simple  $\Delta t$  cut, because the time measurement uncertainties are taken into account.

#### 4. IMPROVEMENT OF THE REJECTION OF THE INTERNAL THALLIUM-208 BACKGROUND

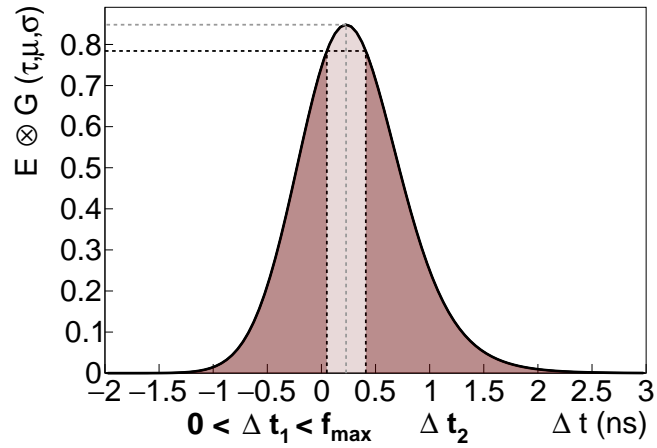
---



(a)  $P_{int} \in [0; 1]$  and  $P_e \in [0; 0.65]$



(b)  $P_{int} \in [0; 0.65]$  and  $P_e \in [0; 1]$



(c)  $P_{int} \in [0.65; 1]$  and  $P_e \in [0.65; 1]$

Figure 4.9:  $E \otimes G$  distributions describing the three areas observed in Fig. 4.8. (a)  $\Delta t^{\text{corr}} \in ]-\infty; 0]$ . (b)  $\Delta t^{\text{corr}} \in ]f_{\text{max}}; +\infty]$ . (c)  $\Delta t^{\text{corr}} \in ]0; f_{\text{max}}]$ .

In the next sub-section, we review how these two cut-offs can be optimised in order to improve the  $^{208}\text{Tl}$  rejection, while keeping a great part of signal events. The final goal is to find optimal cut-offs in order to maximise the 90% CL limit set on  $T_{1/2}^{0\nu}$ .

- relier le point d'inflexion du biplot à ce que l'on voit sur la fig eff 0nu / rej Tl
- Donner le nb d'ev rejeté sur le nb d'ev total, puis sur le nb d'ev retardés

#### 4.4.4 Selection optimisation

### 4.5 Impact of $^{208}\text{Tl}$ rejection on the experiment's sensitivity

Reprendre l'analyse de sensibilité faite avec Axel en rajoutant les cuts Pint/Pexp et delta t pour le final detector

#### 4.5.1 Influence of the calorimeter time resolution

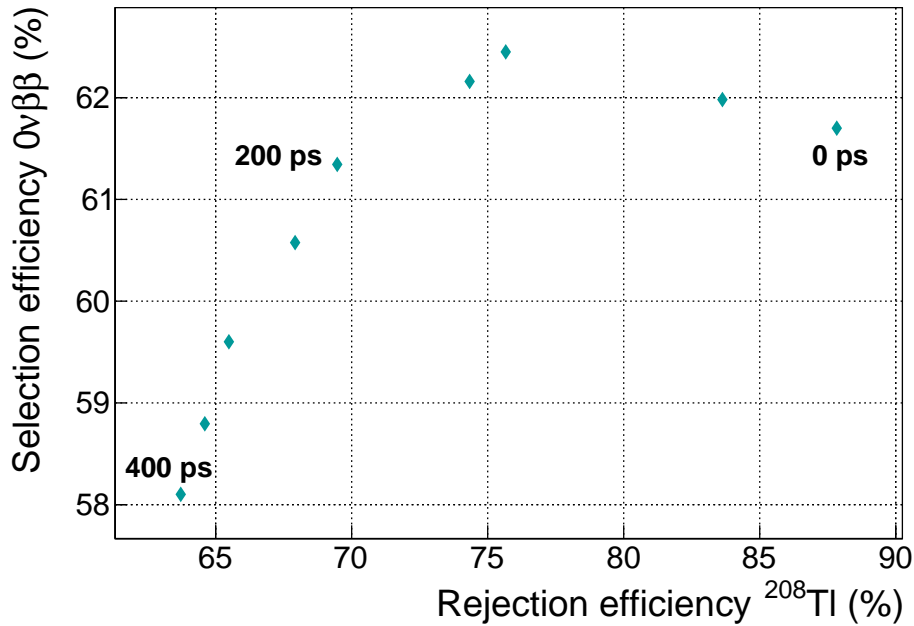


Figure 4.10:  $0\nu\beta\beta$  selection efficiency as a function of  $^{208}\text{Tl}$  rejection efficiency. Each data point corresponds to a given value of  $\sigma_t$ , decrementing in 50 ps steps. First order selections applied on  $0\nu\beta\beta$  and  $^{208}\text{Tl}$  simulations.  $\sigma_l = 27.8$  ps.

- cut efficiencies (delta t et proba) on other backgrounds
- Se servir des résultats de  $\sigma_t$  trouvés au chap. ??

#### 4. IMPROVEMENT OF THE REJECTION OF THE INTERNAL THALLIUM-208 BACKGROUND

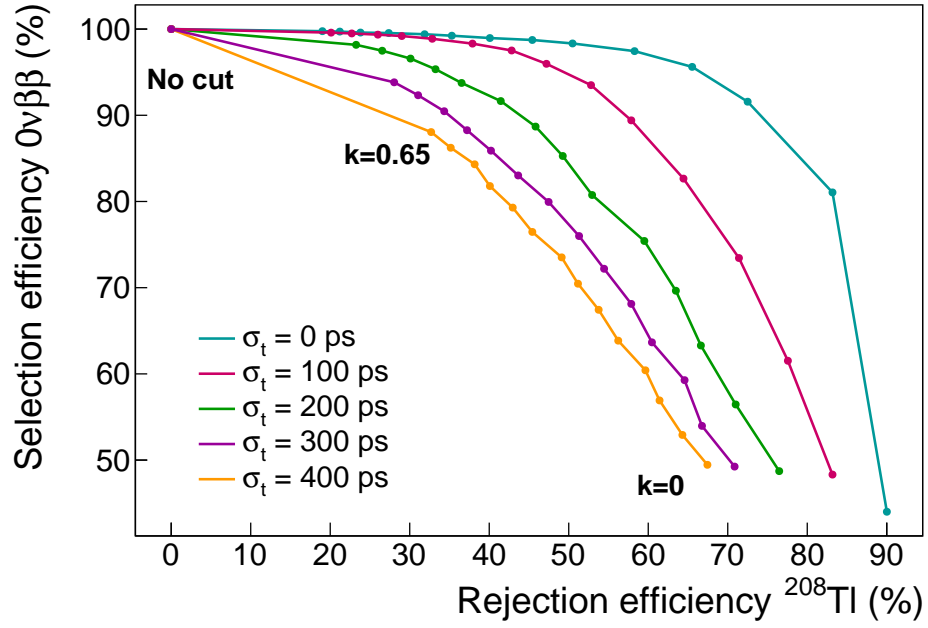


Figure 4.11:  $0\nu\beta\beta$  selection efficiency as a function of  $^{208}\text{Tl}$  rejection efficiency. Each curve corresponds to a given value of  $\sigma_t$ . Each data point corresponds to a minimum value for  $\Delta t$ . First order selections are applied on  $0\nu\beta\beta$  and  $^{208}\text{Tl}$  simulations.  $\sigma_l = 27.8$  ps.

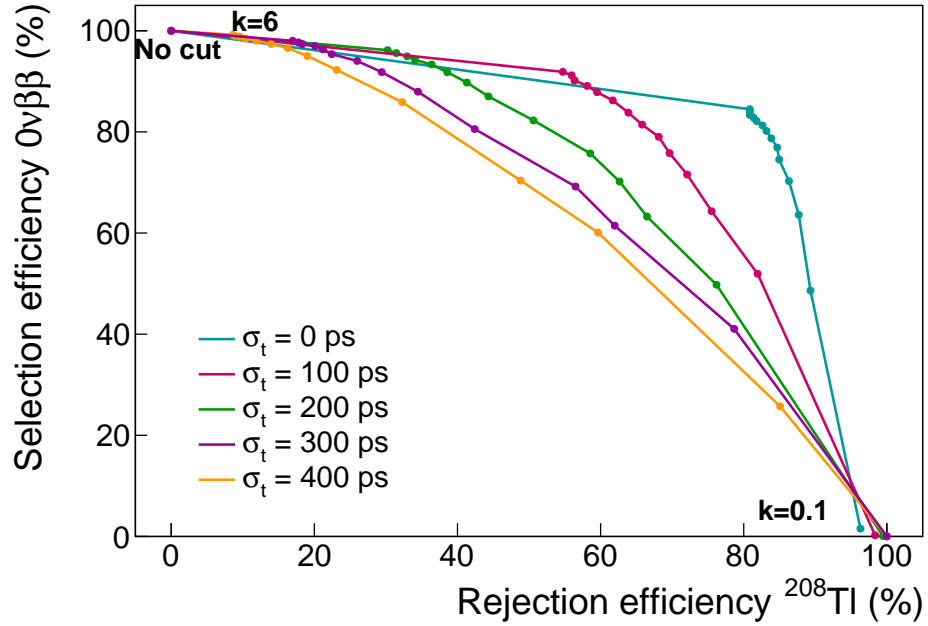


Figure 4.12:  $0\nu\beta\beta$  selection efficiency as a function of  $^{208}\text{Tl}$  rejection efficiency. Each data point corresponds to a given value of  $\sigma_t$ , decrementing in 50 ps steps. First order selections applied on  $0\nu\beta\beta$  and  $^{208}\text{Tl}$  simulations.  $\sigma_l = 27.8$  ps.

- Mais dire que ces sigmas peuvent être améliorés

- donc présenter l'évolution des résultats (efficacité de réjection et sensibilité) sur la réjection en fonction de la valeur de  $\sigma_t$ , à faire varier dans un certain range.
- Tu pourrais avec une figure à 2D où tu montres l'efficacité relative  $0_{nu}$  (égale à 100% avant cette coupure temporelle) en fonction de la réjection du Tl208 -  $\gamma$  cela donne une courbe que tu parcoures et tu cherches à optimiser ton point de fonctionnement.

## 4.6 Conclusions

- On peut éventuellement mettre une source de  $^{232}\text{U}$  dans le détecteur (un des parents de  $^{208}\text{Tl}$ ) pour tester la réjection.
- ajout sélection énergie
- plus correct de couper sur  $P_{exp}$  que sur  $\Delta t$  car on tient compte des erreurs

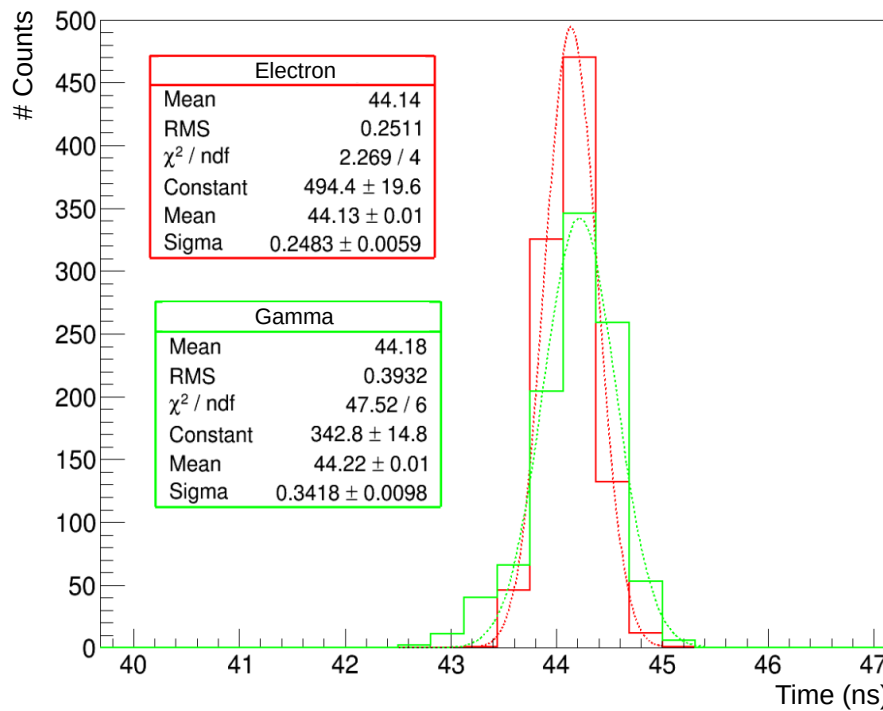


Figure 4.13: Time distribution of the trigger time of an optical module in the case of electrons (red) and gamma radiation (green) depositing an energy of 1 MeV in the scintillator. The trigger threshold is set at 45 mV and corresponds to an energy of 0.150 MeV. Adapted from [?].





---

## Bibliography

- [1] M. Agostini et al. Probing majorana neutrinos with double- $\beta$  decay. *Science* 365, 1445, 2019.
- [2] S.I. Alvis et al. Search for neutrinoless double-beta decay in  $^{76}\text{Ge}$  with 26 kg-yr of exposure from the majorana demonstrator. *Phys. Rev. C*, 100, 2019.
- [3] O. Azzolini et al. First result on the neutrinoless double- $\beta$  decay of  $^{82}\text{Se}$  with cupid-0. *Phys. Rev. Lett.*, 120:232502, Jun 2018.
- [4] C. Alduino et al. First results from cuore: A search for lepton number violation via  $0\nu\beta\beta$  decay of  $^{130}\text{Te}$ . *Phys. Rev. Lett.*, 120:132501, Mar 2018.
- [5] J. B. Albert et al. Search for neutrinoless double-beta decay with the upgraded exo-200 detector. *Phys. Rev. Lett.*, 120:072701, Feb 2018.
- [6] A. Gando et al. Search for majorana neutrinos near the inverted mass hierarchy region with kamland-zen. *Phys. Rev. Lett.*, 117:082503, Aug 2016.
- [7] Nucleid database.
- [8] R. Arnold et al. Probing new physics models of neutrinoless double beta decay with supernemo. *Eur. Phys. J. C*, 2010.
- [9] S. Clavez. *Development of reconstruction tools and sensitivity of the SuperNEMO demonstrator*. PhD thesis, Université Paris Sud, 2017.
- [10] Garrido X. Bongrand M. Hamamatsu 8" pmt test in magnetic shield. Internal presentation, 2014.
- [11] Gomez-Cadenas et al. Physics case of supernemo with  $^{82}\text{Se}$  source. Internal presentation, 2008.
- [12] R. Arnold et al. Final results on  $^{82}\text{Se}$  double beta decay to the ground state of  $^{82}\text{Kr}$  from the nemo-3 experiment. *Eur. Phys. J. C*, 2018.
- [13] Tretyak V.I. Ponkratenko O.A. and Zdesenko Yu.G. The event generator decay4 for simulation of doublebeta processes and decay of radioactive nuclei. *Phys. At. Nucl.*, 63:1282–1287, Jul 2000.

- [14] R. Arnold et al. Results of the search for neutrinoless double- $\beta$  decay in  $^{100}\text{mo}$  with the nemo-3 experiment. *Phys. Rev. D*, 2015.
- [15] Perrot F. Radiopurity measurements for 8" pmts and preliminary budget for the sn demonstrator. Internal presentation, 2017.
- [16] Cousins D. Feldman G. A unified approach to the classical statistical analysis of small signals. *Phys.Rev.*, pages 3873–3889, 1999.
- [17] J. Kotila and F. Iachello. Phase-space factors for double- $\beta$  decay. *Phys. Rev. C*, 85:034316, Mar 2012.
- [18] J. Menéndez et al. Disassembling the nuclear matrix elements of the neutrinoless  $\beta\beta$  decay. *Nuclear Physics A*, 818(3):139 – 151, 2009.
- [19] Y. Iwata et al. Large-scale shell-model analysis of the neutrinoless  $\beta\beta$  decay of  $^{48}\text{Ca}$ . *Phys. Rev. Lett.*, 116:112502, Mar 2016.
- [20] J. Barea, J. Kotila, and F. Iachello.  $0\nu\beta\beta$  and  $2\nu\beta\beta$  nuclear matrix elements in the interacting boson model with isospin restoration. *Phys. Rev. C*, 91:034304, Mar 2015.
- [21] J. Hyvärinen and J. Suhonen. Nuclear matrix elements for  $0\nu\beta\beta$  decays with light or heavy majorana-neutrino exchange. *Phys. Rev. C*, 91:024613, Feb 2015.
- [22] F. Šimkovic et al.  $0\nu\beta\beta$  and  $2\nu\beta\beta$  nuclear matrix elements, quasiparticle random-phase approximation, and isospin symmetry restoration. *Phys. Rev. C*, 87:045501, Apr 2013.
- [23] Tomás R. Egidio J. Luis Vaquero López N., Rodríguez. Shape and pairing fluctuation effects on neutrinoless double beta decay nuclear matrix elements. *Phys. Rev. Lett.*, 111:142501, Sep 2013.
- [24] J. M. Yao, L. S. Song, K. Hagino, P. Ring, and J. Meng. Systematic study of nuclear matrix elements in neutrinoless double- $\beta$  decay with a beyond-mean-field covariant density functional theory. *Phys. Rev. C*, 91:024316, Feb 2015.
- [25] P. K. Rath, R. Chandra, K. Chaturvedi, P. K. Raina, and J. G. Hirsch. Uncertainties in nuclear transition matrix elements for neutrinoless  $\beta\beta$  decay within the projected-hartree-fock-bogoliubov model. *Phys. Rev. C*, 82:064310, Dec 2010.
- [26] Dong-Liang Fang, Amand Faessler, Vadim Rodin, and Fedor Šimkovic. Neutrinoless double- $\beta$  decay of deformed nuclei within quasiparticle random-phase approximation with a realistic interaction. *Phys. Rev. C*, 83:034320, Mar 2011.
- [27] Loaiza P. Source foils measurement with bipo. Internal presentation, 2017.

- [28] Xin Ran Liu. Radon mitigation strategy and results for the supernemo experiment. IoP APP / HEPP Conference, 2018.
- [29] A. Chapon. *Mesure des processus de double désintégration bêta du Mo vers l'état excité  $0_1^+$  du Ru dans l'expérience Nemo3, Programme de R&D SuperNEMO : mise au point d'un détecteur BiPo pour la mesure de très faibles contaminations de feuilles sources*. PhD thesis, Université Caen Basse-Normandie, 2011.
- [30] Snow S. A magnetic field map for the tracker. Internal presentation, 2015.
- [31] A. Pin. *Recherche de la nature du neutrino via la décroissance double bêta sans émission de neutrinos. Caractérisation et optimisation du calorimètre SuperNEMO et impact sur la recherche de la décroissance du  $82\text{Se}$* . Développement du premier prototype LiquidO. PhD thesis, Université Bordeaux-Gradignan, 2020.
- [32] A. H. Wapstra G. Audi. The 1995 update to the atomic mass evaluation. *Nucl. Phys. A*, 595:409–480, feb 1995.
- [33] Dassié D. et al. Two-neutrino double- $\beta$  decay measurement of  $^{100}\text{Mo}$ . *Phys. Rev. D*, 51:2090–2100, Mar 1995.
- [34] R. Arnold et al. Measurement of the  $2\nu\beta\beta$  decay half-life of  $^{150}\text{Nd}$  and a search for  $0\nu\beta\beta$  decay processes with the full exposure from the nemo-3 detector. *Phys. Rev. D*, 94, oct 2016.